10. Bourbonnais, C. & Jérome, D. in *Advances in Synthetic Metals, Twenty Years of Progress in Science and Technology* (eds Bernier, P., Lefrant, S. & Bidan, G.) 206–301 (Elsevier, New York, 1999).
11. Bochrath, M. *et al.* Luttinger-liquid behaviour in carbon nanotubes. *Nature* **397,** 598–601 (1999).
12. Yacoby, A., Stormer, H. L., Baldwin, K. W., Pfeffer, L. N. & West, K. W. Magneto-transport spectroscopy on a quantum wire. *Solid State Commun.* **101,** 77–81 (1995).
13. Heeger, A. J., Kivelson, S., Schrieffer, J. R. & Su, W.-P. Solitons in conducting polymers. *Rev. Mod. Phys.* **60,** 781–850 (1988).
14. Djurek, D., Prester, M., Jérome, D. & Bechgaard, K. Magnetic field dependent thermal conductivity in the organic superconductor $(TMTSF)_2ClO_4$. *J. Phys. C* **15,** L669–L674 (1982).
15. Choi, M.-Y., Chaikin, P. M. & Greene, R. L. Thermal conductivity of bis-tetramethyltetraselenafulvalen perchlorate [$(TMTSF)_2ClO_4$]. *Phys. Rev. B* **34,** 7727–7732 (1986).
16. Coulon, C. *et al.* A new survey of the physical properties of the $(TMTTF)_2X$ series. Role of the counterion ordering. *J. Phys.* **43,** 1059–1067 (1982).
17. Berman, R. *Thermal Conduction in Solids* (Clarendon, Oxford, 1976).
18. Slack, G. A. in *Solid State Physics* Vol. 34 (eds Ehrenreich, H., Seitz, F. & Turnbull, D.) 1–71 (Academic, New York, 1979).
19. Sologubenko, A. V., Gianno, K., Ott, H. R., Ammerahl, U. & Revcolevschi, A. Thermal conductivity of the hole-doped spin ladder system $Sr_{14-x}Ca_xCu_{24}O_{41}$. *Phys. Rev. Lett.* **84,** 2714–2717 (2000).
20. Sologubenko, A. V., Giannò, K., Ott, H. R., Vietkine, A. & Revcolevschi, A. Heat transport by lattice and spin excitations in the spin-chain compounds $SrCuO_2$ and Sr_2CuO_3. *Phys. Rev. B* **64,** 054412-1–054412-11 (2001).
21. Dumm, M. *et al.* Electron spin resonance studies on the organic linear-chain compound $(TMTCF)_2X$ (C = S,Se; X = PF_6,AsF_6,ClO_4,Br). *Phys. Rev. B* **61,** 511–520 (2000).
22. Klümper, A. The spin-1/2 Heisenberg chain: thermodynamics, quantum criticality and spin-peierls exponents. *Eur. Phys. J. B* **5,** 677–685 (1998).
23. Schwarz, A. *et al.* On-chain electrodynamics of metallic $(TMTSF)_2X$ salts: Observation of Tomonaga-Luttinger liquid response. *Phys. Rev. B* **58,** 1261–1271 (1998).
24. Claessen, R. *et al.* Spectroscopic signature of spin-charge separation in the quasi-one-dimensional organic conductor TTF-TCNQ. *Phys. Rev. Lett.* **88,** 096402-1–096402-4 (2002).
25. Zeini, B. *et al.* Thermal conductivity and thermal Hall effect in Bi- and Y-based high-T_c superconductors. *Eur. Phys. J. B* **20,** 189–208 (2001).
26. Engelsberg, S. & Varga, B. B. One-dimensional electron-photon model. *Phys. Rev.* **136,** A1582–A1589 (1964).

Acknowledgements

We thank M. Braden, C. Hess, J. Jérome, A.P. Kampf, D.I. Khomskii, E. Müller-Hartmann, H.R. Ott and G.A. Sawatzky for discussions. This work was supported by the Deutsche Forschungsgemeinschaft and by the VolkswagenStiftung.

Competing interests statement

The authors declare that they have no competing financial interests.

Correspondence and requests for materials should be addressed to A.F. (e-mail: freimuth@ph2.uni-koeln.de).

Sub-ångstrom resolution using aberration corrected electron optics

P. E. Batson*, N. Dellby† & O. L. Krivanek†

** IBM Thomas J. Watson Research Center, Yorktown Heights, New York 10598, USA*
† Nion R&D, Kirkland, Washington 98033, USA

Following the invention of electron optics during the 1930s, lens aberrations have limited the achievable spatial resolution to about 50 times the wavelength of the imaging electrons[1]. This situation is similar to that faced by Leeuwenhoek in the seventeenth century, whose work to improve the quality of glass lenses led directly to his discovery of the ubiquitous "animalcules" in canal water, the first hints of the cellular basis of life. The electron optical aberration problem was well understood from the start, but more than 60 years elapsed before a practical correction scheme for electron microscopy was demonstrated[2], and even then the remaining chromatic aberrations still limited the resolution. We report here the implementation of a computer-controlled aberration correction system in a scanning transmission electron microscope[3], which is less sensitive to chromatic aberration. Using this approach, we achieve an electron probe smaller than 1 Å. This performance, about 20 times the electron wavelength at 120 keV energy, allows dynamic imaging of single atoms, clusters of a few atoms, and single atomic layer 'rafts' of atoms coexisting with Au islands on a carbon substrate. This technique should also allow atomic column imaging of semiconductors, for detection of single dopant atoms, using an electron beam with energy below the damage threshold for silicon.

Over 50 years ago, Scherzer[1] recognized that round electron lenses would suffer from spherical aberration, limiting spatial resolution in an electron microscope to about 2 Å for electrons of energy 100–200 keV. This is unfortunate, because at this resolution the atomic structure of most crystalline materials can be imaged in only one projection. Improving the resolution to 0.5 Å would increase the number of available crystal projections to more than twelve, allowing three-dimensional imaging of atomic structure. This problem is illustrated by the recent detection of individual dopant atoms within bulk semiconductors[4], where structural characterization of the local environment of the dopant atoms was complicated by the 1.6-Å probe size, slightly larger than the 1.36-Å distance between atoms in the {110} projection of Si.

Scherzer also pointed out three possible ways to correct the limiting aberrations: (1) use of non-round lenses; (2) use of lenses

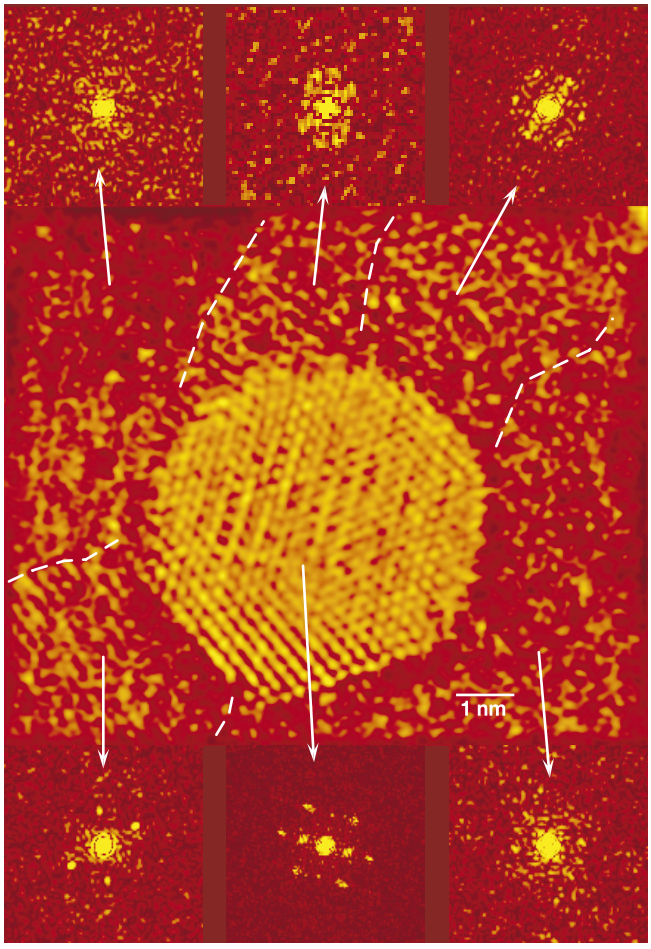

Figure 1 Atomic resolution image of a Au island on an amorphous carbon substrate. Surrounding the island are 'rafts' of single atomic layers of Au. Further away, small clusters and single atoms of Au are present. Diffraction patterns from various regions surrounding the island show that the rafts are ordered in various structures adjacent to the built-up islands.

with charge on axis (including mirrors); and (3) use of time-varying fields. Since his work, many attempts have been made to develop practical aberration correctors for the transmission electron microscope (TEM), culminating in the successful work of Haider *et al.* in the 1990s (ref. 2), which was the first to demonstrate a resolution improvement in a particular instrument. Difficulties remain, however, because the TEM requires a faithful treatment of electron paths which are far from the optic axis, necessitating chromatic aberration correction or addition of an electron monochromator, a task which is not yet complete.

In the late 1960s, an alternative to the TEM imaging geometry was introduced by Crewe *et al.*[3]. They used similar optics to produce a very small electron probe that was scanned in a raster over the area of interest. This geometry, called the scanning transmission electron microscope (STEM), has become an important tool for quantitative microscopy because many types of analytical signals can be used to produce an image of the scanned area. In particular, annular dark field (ADF) imaging, using high-angle elastic scattering which occurs near individual atoms[5], has emerged as the primary imaging technique. ADF STEM imaging enjoys several advantages over conventional TEM imaging: (1) the spatial resolution is somewhat better; (2) it is sensitive to the atomic number of the imaged atoms; and (3) it provides a positive definite transfer of specimen spatial frequencies, allowing a direct interpretation of results with fewer ambiguities. As the resolution of instruments has improved, ADF imaging has made important contributions to the imaging of individual columns of atoms in crystals[6,7] and, more recently, to the single dopant atom detection within the bulk[4]. The STEM is also compatible with other analytical techniques, including electron energy loss spectroscopy (EELS)[8]. This technique has proved especially powerful, producing atomic resolution information about atomic species, bonding environment and local electronic structure[9–11].

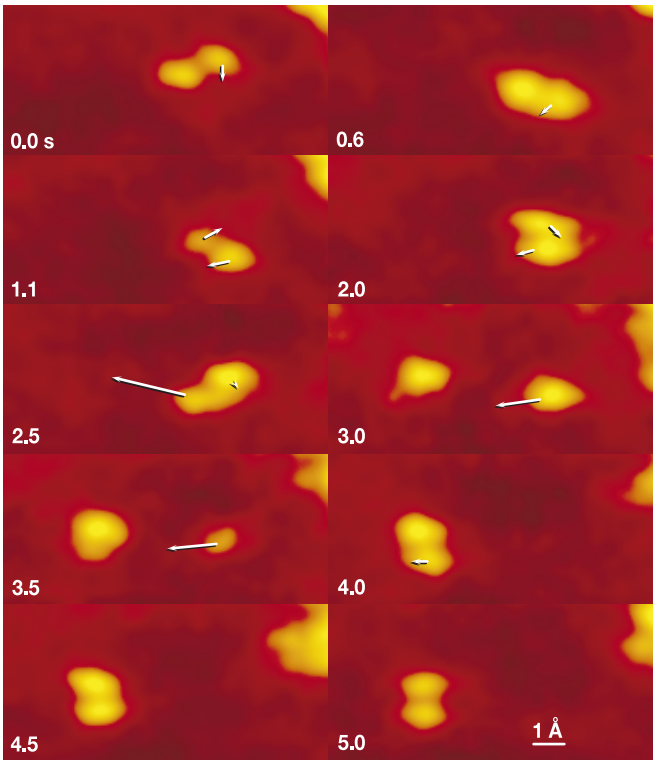

Figure 2 Selected frames from a 10 frames s^{-1} acquisition of the interaction of two Au atoms. The interaction is clearly attractive beyond about 1.5 Å and repulsive at smaller distances. Motion occurs in fast jumps, indicated by the arrows, with relatively long periods at rest. At 3.5 s in this sequence, a jump appears to occur within one frame.

The instrument used in this work is based on the VG Microscopes HB501 STEM with the addition of a quadrupole–octupole aberration corrector[12]. Before the incorporation of the corrector, the IBM STEM had been used extensively for ADF imaging and spatially resolved EELS of defects and interfaces in semiconductors[9]. At the 1.9-Å resolution level, it yielded tantalizing, but incomplete information about the atomic structure of important defects such as the dissociated 60° dislocation in Si-Ge/Si structures[13]. The corrector comprises seven major elements: four quadrupoles separated by three octupoles. In addition, minor windings include dipoles and quadrupoles at each stage to allow the control of parasitic aberrations. In all, 35 windings are excited separately using 0.3 p.p.m. stability, computer-controlled current supplies. All axial aberrations up to fifth order in angle are determined by software which analyses electron shadow images (Ronchigrams[14]) obtained by a television camera located in the far field behind the specimen. The software then adjusts the corrector to compensate for aberrations up to fourth order. The system spherical aberration (third order) is finally adjusted to about $-50\,\mu m$ to optimally oppose the effects of fifth order aberrations, which are not corrected in the present instru-

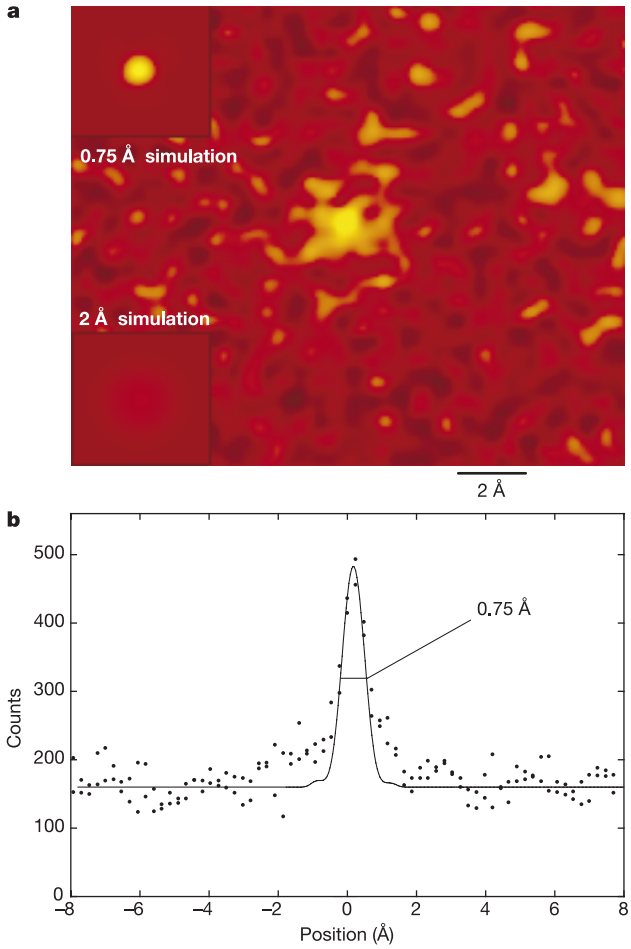

Figure 3 An analysis of the image size of a single Au atom. **a**, Image of a single Au atom on a carbon support compared with simulations for the corrected (upper inset) and uncorrected (lower inset) instrument. The upper inset, showing 0.75 Å resolution, is a full calculation for the ADF STEM using the Au projected potential, the measured aberration coefficients, and a source size of 0.3 Å, estimated using the source brightness (about 10^9 Å cm^{-2} sr^{-1}), the measured probe current (40 pA) and the 50 mrad full illumination angle. The atom would not be visible at the 1.9 Å resolution, shown in the lower left, obtained for a spherical aberration coefficient of 1.2 mm in the uncorrected instrument. **b**, Line scan data, obtained from the image, are compared with the 0.75 Å probe calculation.

ment. Details are described elsewhere[12].

Preliminary imaging of 100-Å Au islands on amorphous carbon have yielded many images similar to that shown in Fig. 1. We see, in addition to the islands, a hierarchy of structures: flat areas with no apparent Au atoms, single atoms, clusters of 2–3 atoms, and 20–50-Å-wide single layer rafts of Au atoms. We identify them as Au layers on the basis of the similarity of their image contrast with that of single atoms produced during dissolution of small Au islands. The monolayer rafts appear to be transition regions between the islands and the more sparsely occupied areas further away, and so we speculate that they may be important to the exchange of atoms between the island and the substrate during growth[15]. Finally, the single atom contrast was high enough to follow the motion of atoms under the electron beam, during dissolution of islands and during rapid reformation of islands from dilute groups of atoms.

Figure 2 summarizes a 10 frames s^{-1} acquisition of the interaction between two Au atoms at 300 K on the carbon surface. An attractive interaction is clearly visible when the separation is greater than about 1.3–1.5 Å, but at no time do the Au atoms approach closer than this. In this sequence, the two atoms approach, circle one another, separate by about 4 Å and then rejoin. Several things need to be investigated to understand this process: (1) the substrate is complex, possibly providing low-energy channels for atomic motion; (2) the electron beam imparts a finite impulse to the atoms during the imaging process, but the magnitude of this impulse relative to thermal fluctuations needs to be evaluated; (3) higher-speed acquisition may provide information about the diffusion velocity in this situation.

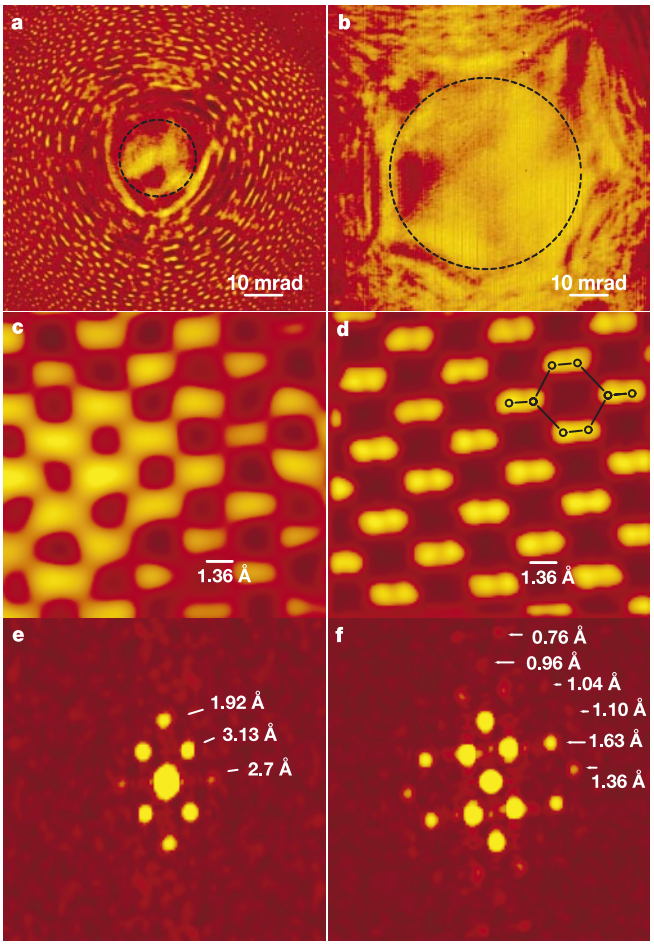

Figure 4 Summary of results for the {110} projection of $Ge_{30}Si_{70}$. **a**, **b**, Ronchigram shadow maps for uncorrected and corrected imaging. Circles indicate the range of angles used for probe formation. **c**, **d**, Images of the {110} projection of the crystal obtained using the conditions in **a** and **b**. Lines and circles indicate the projected atomic structure. The image on the left is the result of a sum of several 0.5-s acquisitions, while that on the right is a sum of several sections cut from a single large area image obtained in 0.5-s, using a beam current of about 40 pA. **e**, **f**, The Fourier power spectra for the two examples in **c** and **d**. Spatial frequencies are marked.

Fourier transform power spectra for the images such as Fig. 1 show spatial frequencies as small as 1.17 Å, but this does not give us a good measure of the probe size for several reasons. For instance, small crystal tilts in the islands can lead to blurring of the atom columns. Errors in acquisition of the image intensity, particularly in the low-intensity region between atom columns in crystals, can lead to nonphysical spatial periodicities (Yu, Z. and Silcox, J., personal communication). Therefore, we have used images of single Au atoms to evaluate the probe size. This evaluation is summarized in Fig. 3a, where we show an image of a single Au atom compared with calculated images for the corrected and uncorrected instrument. We estimate the probe shape on the basis of the measured system aberration parameters, obtained from an analysis of the electron shadow map at the time of the experiment, and the finite source size, obtaining a corrected probe size of 0.74 Å and an uncorrected size of 1.9 Å at 120 keV. Using a full ADF STEM image calculation for the Au atom[16], we obtain a corrected image width of 0.75 Å. The visual correspondence is good, but more interestingly, it is obvious that the 1.9 Å resolution is not good enough even to detect single Au atoms in the presence of noise from the carbon support. In Fig. 3b, we compare the 0.75 Å profile with data obtained from the atom image. Although the statistical quality for the experiment is not sufficient to obtain much detail regarding the shape of the image, certainly the width is consistent with the calculated width.

Figure 4 shows results for a $Ge_{30}Si_{70}$ alloy with and without aberration correction. The shadow maps in Fig. 4a and b show regions of minimum contrast at the centre defining an area of constant electron phase, appropriate for use in forming a small probe. The larger available area using aberration correction produces the smaller probe, consistent with the Heisenberg uncertainty relation. Figure 4c and d shows the resulting crystal image. Markers highlight the well-known 1.36 Å 'dumb-bell' structure formed by the near-neighbour atom columns. In Fig. 4e and f the spatial power spectra for the images is shown. In the uncorrected result, a few spacings out to 1.92 Å are present, illustrating the best previous performance. In the corrected result, many spacings are present, including {551} planes with 0.76 Å spacings. This is a great improvement over that achieved in the past in essentially the same instrument[12]. We caution, however, that care needs to be applied in interpreting this image because high spatial frequencies can be induced by nonlinearities in the image acquisition (Yu, Z. and Silcox, J., personal communication). This has not been observed in the past at 1.9 Å resolution, but does appear to be present at some level in the new results. Even so, the dramatic contrasts between the images are obvious.

To our knowledge, no other electron microscope has attained sub-ångstrom directly interpretable resolution in a single image. Lattice spacings smaller than 1 Å have been observed using high beam energy[17], and sub-ångstrom resolution has been obtained by *a posteriori* processing[18]. However, the electron phases in the raw data in such work are always severely distorted, and no structural conclusions are possible without extensive computer processing. Moreover, the acquisition for this approach can exceed one hour, thus exacerbating beam damage, particularly for light elements. Structural resolution much better than 1 Å can also be obtained from electron diffraction data[19]. However, this approach is limited to periodic structures, and also requires extensive computer processing.

This successful aberration correction is linked to recent technical advances: (1) computation of electron optical parameters is now

possible for nonrotationally symmetric systems, allowing practical designs to be simulated with high accuracy; (2) mechanical fabrication tolerances have advanced materially in the past 15 years; (3) high stability electronic components have become available in the past 10 years, allowing the packaging of many, very high stability, computer-controlled power supplies in a small space; and (4) high-speed small computers are now available for real-time processing of the shadow map Rochigram data to obtain aberration parameters.

We believe aberration correction technology combined with the inherent power of the STEM instrument opens the way for lower voltage, smaller, 'smarter', more easily managed instruments that will be capable of routinely imaging and analysing materials at sub-ångstrom resolution, using several different crystal orientations. Specialized instruments, perhaps using some submillimetre-sized electrostatic imaging elements, may reach the diffraction limit for the imaging electrons. Multiple corrector systems will allow aberration control of both probe size and detector field of view, in a manner somewhat similar to confocal light microscopy. Finally, detailed control of the amplitude and phase of the incident and scattered electron wavefunction will be possible, allowing specific specimen inelastic transitions to be accessed[20]. Thus aberration correction marks a shift towards precise optical control that will allow routine atomic level characterization of defects and interfaces within bulk materials. □

Received 5 April; accepted 4 July 2002; doi:10.1038/nature00972.

1. Scherzer, O. The theoretical resolution limit of the electron microscope. *J. Appl. Phys.* **20,** 20–29 (1949).
2. Haider, M., Uhlemann, S., Schwan, E., Kabius, B. & Urban, K. Electron microscopy image enhanced. *Nature* **392,** 768–769 (1998).
3. Crewe, A. V., Isaacson, M. & Johnson, D. A simple scanning electron microscope. *Rev. Sci. Instrum.* **40,** 241–246 (1969).
4. Voyles, P. M., Muller, D. A., Grazul, J. L., Citrin, P. H. & Gossmann, H.-J. L. Atomic-scale imaging of individual dopant atoms and clusters in highly n-doped bulk Si. *Nature* **416,** 826–829 (2002).
5. Crewe, A. V., Wall, J. & Langmore, J. Visibility of a single atom. *Science* **168,** 1338–1340 (1970).
6. Pennycook, S. J. & Boatner, L. A. Chemically sensitive structure-imaging with a scanning transmission electron microscope. *Nature* **336,** 565–567 (1988).
7. Xu, P., Kirkland, E. J., Silcox, J. & Keyse, R. High resolution imaging of silicon (111) using a 100 KeV STEM. *Ultramicroscopy* **32,** 93–102 (1990).
8. Crewe, A. V., Isaacson, M. & Johnson, D. A high resolution electron spectrometer for use in transmission scanning microscopy. *Rev. Sci. Instrum.* **42,** 411–420 (1971).
9. Batson, P. E. Simultaneous STEM imaging and electron-energy-loss-spectroscopy with atomic-column sensitivity. *Nature* **366,** 727–728 (1993).
10. Muller, D. A., Tzou, Y., Raj, R. & Silcox, J. High resolution EELS at grain boundaries. *Nature* **366,** 725–727 (1993).
11. Browning, N. D., Chisholm, M. F. & Pennycook, S. J. Atomic resolution analysis using a scanning transmission electron microscope. *Nature* **366,** 143–146 (1993).
12. Dellby, N., Krivanek, O. L., Nellist, P. D., Batson, P. E. & Lupini, A. R. Progress in aberration-corrected scanning transmission electron microscopy. *J. Electron. Microsc.* **50,** 177–185 (2001).
13. Batson, P. E. Structural and electronic characterization of a dissociated 60° dislocation in GeSi. *Phys. Rev. B* **61,** 16633–16641 (2000).
14. Ronchi, V. Forty years of history of a grating interferometer. *Appl. Opt.* **3,** 437–450 (1964).
15. Zhang, Z. Y. & Lagally, M. G. Atomistic processes in the early stages of thin film growth. *Science* **276,** 377–383 (1997).
16. Kirkland, E. J. *Advanced Computing in Electron Microscopy* (Plenum, New York, 1998).
17. Kawasaki, T. *et al.* Development of a 1 MV field emission transmission electron microscope. *J. Electron. Microsc.* **49,** 711–718 (2000).
18. O'Keeffe, M. A. *et al.* Sub-ångstrom high resolution transmission electron microscopy at 300 keV. *Ultramicroscopy* **89,** 215–241 (2001).
19. Zuo, J., Kim, Y., O'Keeffe, M. & Spence, J. C. H. Direct observation of d holes and Cu-Cu bonding in Cu_2O. *Nature* **401,** 49–56 (1999).
20. Batson, P. E. Symmetry selected electron energy loss scattering in diamond. *Phys. Rev. Lett.* **70,** 1822–1825 (1993).

Acknowledgements

O.L.K. and N.D. acknowledge partial support for this project from the IBM Corporation.

Competing interests statement

The authors declare that they have no competing financial interests.

Correspondence and requests for materials should be addressed to P.E.B. (e-mail: batson@us.ibm.com).

Experimental evidence for sub-3-fs charge transfer from an aromatic adsorbate to a semiconductor

Joachim Schnadt*, Paul A. Brühwiler*, Luc Patthey†, James N. O'Shea*, Sven Södergren*, Michael Odelius‡, Rajeev Ahuja*, Olof Karis*, Margit Bässler§, Petter Persson*, Hans Siegbahn*, S. Lunell* & Nils Mårtensson§*

* *Department of Physics, Uppsala University, Box 530;* ‡ *Department of Physical Chemistry, Uppsala University, Box 532, 75121 Uppsala, Sweden*
† *Swiss Light Source, Paul-Scherrer-Institut, 5232 Villigen-PSI, Switzerland*
§ *MAX-Lab, University of Lund, Box 118, 22100 Lund, Sweden*

The ultrafast timescale of electron transfer processes is crucial to their role in many biological systems and technological devices. In dye-sensitized solar cells[1–4], the electron transfer from photo-excited dye molecules to nanostructured semiconductor substrates needs to be sufficiently fast to compete effectively against loss processes and thus achieve high solar energy conversion efficiencies[4]. Time-resolved laser techniques indicate an upper limit of 20 to 100 femtoseconds[5–9] for the time needed to inject an electron from a dye into a semiconductor, which corresponds to the timescale on which competing processes such as charge redistribution[10,11] and intramolecular thermalization of excited states[12–14] occur. Here we use resonant photoemission spectroscopy, which has previously been used to monitor electron transfer in simple systems with an order-of-magnitude improvement in time resolution[15,16], to show that electron transfer from an aromatic adsorbate to a TiO_2 semiconductor surface can occur in less than 3 fs. These results directly confirm that electronic coupling of the aromatic molecule to its substrate is sufficiently strong to suppress competing processes[17].

The most efficient photoelectrochemical solar cells are currently based on a nanostructured TiO_2 electrode[3]. The electrode is sensitized to visible light by adsorption of a dye. One of the most promising dyes is "N3"[18] or $(dcb)_2Ru(NCS)_2$ (dcb = 4,4′-dicarboxy-2,2′-bipyridine, also termed bi-isonicotinic acid), which binds to the nanostructured electrode through one[19] or two[1] dcb

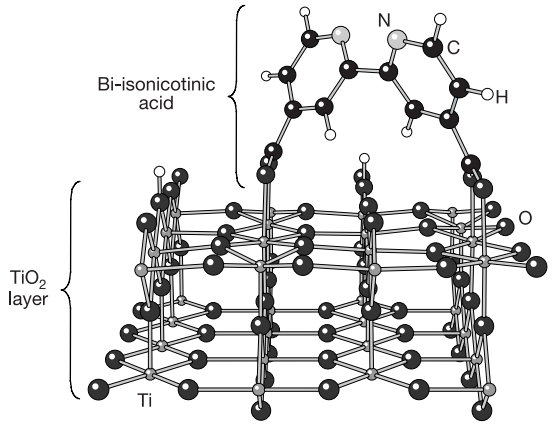

Figure 1 Geometry of the adsorption structure of bi-isonicotinic acid on TiO_2(110). The bonding is on-top for each oxygen atom (2M-bidentate) in both carboxyl groups, with the dissociated hydrogen atoms (small white spheres) assumed to bond to nearby surface oxygen atoms. The pyridine rings are tilted in opposite directions around the inter-ring bond (large white spheres, nitrogen; large black spheres, carbon). The structural model was further refined for the present study using first-principles plane-wave density functional calculations and performing a full optimization of the adsorbate and the surface TiO_2 layer (small white spheres, titanium; large black spheres, oxygen).

analysed as described[10], with a final FIXa concentration of 1 nM. All data presented is the mean ± s.e.m. for at least three independent experiments.

Enzyme assays

Factor VIII (Hemophil M, Baxter Healthcare) was activated with thrombin, then the FVIIIa solution was added to factor IXa and phospholipid vesicles (lipids purchased from Avanti Polar Lipids and vesicles prepared as in ref. 28) and allowed to form the FIXa–FVIIIa enzyme complex. Factor X and aptamer were then added, and factor X activation measured with a chromogenic substrate (Pefachrome fXa, Centerchem Inc.). Final concentrations were: factor IXa, 0.2 nM; factor VIIIa, 0.7 nM; lipid, 40 μM; factor X, 135 nM; and factor Xa substrate, 1 mM. The rate of factor Xa generation was determined by a second-order fit to the data. The %FX cleavage activity is 100 times the rate of FXa generation in the presence of aptamer divided by rate in the absence of aptamer.

Clotting assays

Activated partial thromboplastin time (APTT) assays were performed using a model ST4 mechanical coagulometer (Diagnostica Stago Inc.). Aptamer in binding buffer (5 μl) without BSA or binding buffer without BSA alone was added to pooled normal human plasma (50 μl) (George King Biomedical), and incubated for 5 min at 37 °C. MDA platelin (50 μl) (bioMerieux) was then added and allowed to activate the plasma for 5 min, followed by the addition of 25 mM $CaCl_2$ (50 μl) to initiate the clotting reaction. Data is expressed as the relative change in clot time; the clot time in the presence of aptamer divided by the clot time in the presence of buffer alone. All reactions were performed in duplicate, and only duplicates differing by <10% were used in analysis.

Prothrombin time (PT) clotting assays were performed as previously described[7] except that 5 μl of aptamer was added to 50 μl of normal pooled human plasma, and all reactions were carried out at 37 °C.

Antidote assays

Antidote oligonucleotides were synthesized and purified by Dharmacon Research, Inc. Antidote activity was measured 10 min after antidote addition to plasma containing aptamer in APTT clotting assays. Briefly, human plasma was anticoagulated with aptamer, antidote oligonucleotide (5 μl) was added and the incubation continued for 5 min before the addition of MDA platelin. Antidote activity is expressed as the per cent residual anticoagulant activity T of the aptamer, which is:

$$[1 - (T_{\text{aptamer alone}} - T_{\text{aptamer+antidote}})/(T_{\text{aptamer alone}} - T_{\text{baseline}})] \times 100.$$

For measuring the kinetics of the onset of antidote activity, the incubation time of the plasma following MDA platelin addition was reduced to 1 min to allow for shorter timepoints to be measured. This increased the baseline APTT from 30.2–32.5 s to 34.2–36.8 s.

Gel shift assays were performed essentially as described[29]. Aptamer 9.3t (50 nM with trace ^{32}P-labelled) was incubated for 10 min with varying concentrations of antidote oligonucleotide in binding buffer without BSA before loading on a 12% polyacrylamide gel containing 2 mM $CaCl_2$. Gels were run for 3 h at 300 V and visualized using a Storm 840 Phosphorimager (Molecular Dynamics).

Patient samples

Plasma samples from six patients with HIT were studied. Clinical criteria for the diagnosis of HIT included thrombocytopenia and/or new or recurrent thrombosis after five or more days of heparin therapy[5]. Serologic criteria included a positive heparin-induced platelet aggregation assay and/or elevated heparin/platelet factor 4 antibody levels detected by enzyme-linked immunosorbent assay (ELISA) (GTI Inc.). Five patients met both clinical and serologic criteria; one patient fulfilled clinical criteria but had negative serologic studies. The Institutional Review Board at Duke University Medical Center approved these studies, and informed consent was obtained from all patients.

Received 12 February; accepted 18 June 2002; doi:10.1038/nature01058.

1. Levine, M. N., Raskob, G., Landefeld, S. & Kearon, C. Hemorrhagic complications of anticoagulant treatment. *Chest* **119,** 108S–121S (2001).
2. Hirsch, J., Anand, S. S., Halperin, J. L. & Fuster, V. Guide to anticoagulant therapy: Heparin: A statement for healthcare professionals from the American Heart Association. *Circulation* **103,** 2994–3018 (2001).
3. Carr, J. A. & Silverman, N. The heparin-protamine interaction. A review. *J. Cardiovasc. Surg.* **40,** 659–666 (1999).
4. Pifarre, R., Walenga, J. M. & Fareed, J. in *New Anticoagulants for the Cardiovascular Patient* (ed. Pifarre, R.) 1–7 (Hanley and Belfus, Philadelphia, 1997).
5. Warkentin, T. E., Chong, B. H. & Greinacher, A. Heparin-induced thrombocytopenia: towards consensus. *Thromb. Haemost.* **79,** 1–7 (1998).
6. Johnson, K. & Hung, D. Novel anticoagulants based on inhibition of the factor VIIa/tissue factor pathway. *Coron. Artery Dis.* **9,** 83–87 (1998).
7. Rusconi, C. P., Yeh, A., Lyerly, H. K., Lawson, J. H. & Sullenger, B. A. Blocking the initiation of coagulation by RNA aptamers to factor VIIa. *Thromb. Haemost.* **84,** 841–848 (2000).
8. Bock, L. C., Griffin, L. C., Latham, J. A., Vermaas, E. H. & Toole, J. J. Selection of single-stranded DNA molecules that bind and inhibit human thrombin. *Nature* **355,** 564–566 (1992).
9. Tasset, D. M., Kubik, M. F. & Steiner, W. Oligonucleotide inhibitors of human thrombin that bind distinct epitopes. *J. Mol. Biol.* **272,** 688–698 (1997).
10. White, R. *et al.* Generation of species cross-reactive aptamers using "toggle" SELEX. *Mol. Ther.* **4,** 567–573 (2001).
11. Tuerk, C. & Gold, L. Systematic evolution of ligands by exponential enrichment: RNA ligands to bacteriophage T4 DNA polymerase. *Science* **249,** 505–510 (1990).
12. Ellington, A. D. & Szostak, J. W. *In vitro* selection of RNA molecules that bind specific ligands. *Nature* **346,** 818–822 (1990).
13. Pieken, W. A., Olsen, D. B., Benseler, F., Aurup, H. & Eckstein, F. Kinetic characterization of ribonuclease-resistant 2′-modified hammerhead ribozymes. *Science* **253,** 314–317 (1991).
14. Davis, J. P., Janjic, N., Javornik, B. E. & Zichi, D. A. Identifying consensus patterns and secondary structure in SELEX sequence sets. *Methods Enzymol.* **267,** 302–314 (1996).
15. Watson, S. R. *et al.* Anti-L-selectin aptamers: binding characteristics, pharmacokinetic parameters, and activity against an intravascular target in vivo. *Antisense Nucleic Acid Drug Dev.* **10,** 63–75 (2000).
16. Tucker, C. E. *et al.* Detection and plasma pharmacokinetics of an anti-vascular endothelial growth factor oligonucleotide-aptamer (NX1838) in rhesus monkeys. *J. Chromatogr. B Biomed. Sci. Appl.* **732,** 203–212 (1999).
17. High, K. A. & Roberts, H. R. in *Molecular Basis of Thrombosis and Hemostasis* (eds High, K. A. & Roberts, H. R.) 215–237 (Marcel Dekker, New York, 1995).
18. Spanier, T. B. *et al.* Selective anticoagulation with active site-blocked factor IXA suggests separate roles for intrinsic and extrinsic coagulation pathways in cardiopulmonary bypass. *J. Thorac. Cardiovasc. Surg.* **116,** 860–869 (1998).
19. Feuerstein, G. Z. *et al.* An inhibitory anti-factor IX antibody effectively reduces thrombus formation in a rat model of venous thrombosis. *Thromb. Haemost.* **82,** 1443–1445 (1999).
20. Choudhri, T. F. *et al.* Targeted inhibition of intrinsic coagulation limits cerebral injury in stroke without increasing intracerebral hemorrhage. *J. Exp. Med.* **190,** 91–99 (1999).
21. White, R. R., Sullenger, B. A. & Rusconi, C. P. Developing aptamers into therapeutics. *J. Clin. Invest.* **106,** 929–934 (2000).
22. Campbell, K. R. *et al.* Bivalirudin in patients with heparin-induced thrombocytopenia undergoing percutaneous coronary intervention. *J. Invasive Cardiol.* **12,** 14F–19F (2000).
23. Greinacher, A. *et al.* Recombinant hirudin (lepirudin) provides safe and effective anticoagulation in patients with heparin-induced thrombocytopenia: a prospective study. *Circulation* **99,** 73–80 (1999).
24. Lewis, B. E. *et al.* Argatroban anticoagulant therapy in patients with heparin-induced thrombocytopenia. *Circulation* **103,** 1838–1843 (2001).
25. Hicke, B. J. & Stephens, A. W. Escort aptamers: a delivery service for diagnosis and therapy. *J. Clin. Invest.* **106,** 923–928 (2000).
26. van Dijk, M. A. & van de Winkel, J. G. Human antibodies as next generation therapeutics. *Curr. Opin. Chem. Biol.* **5,** 368–374 (2001).
27. Fitzwater, T. & Polisky, B. A SELEX primer. *Methods Enzymol.* **267,** 275–301 (1996).
28. Hope, M. J., Bally, M. B., Webb, G. & Cullis, P. R. Production of large unilamellar vesicles by a rapid extrusion procedure. Characterization of size distribution, trapped volume and ability to maintain a membrane potential. *Biochim. Biophys. Acta* **812,** 55–65 (1985).
29. Silverman, S. K. & Cech, T. R. Energetics and cooperativity of tertiary hydrogen bonds in RNA structure. *Biochemistry* **38,** 8691–8702 (1999).

Acknowledgements

We thank R. Califf and R. Harrington for their insight into the need for antidote-controlled anticoagulant and antithrombotic agents. This work was supported by grants from the American Heart Association to C.P.R. and the National Institutes of Health to B.A.S, T.L.O. and D.M.

Competing interests statement

The authors declare competing financial interests: details accompany the paper on *Nature*'s website (http://www.nature.com/nature).

Correspondence and requests for materials should be addressed to C.P.R. (e-mail: c.rusconi@cgct.duke.edu) or B.A.S. (e-mail: b.sullenger@cgct.duke.edu).

corrigendum

Sub-ångstrom resolution using aberration corrected electron optics

P. E. Batson, N. Dellby & O. L. Krivanek

Nature **418**, 617–620 (2002).

For this Letter the disclosure form for the declaration of competing financial interests was incorrectly filled out because of a misunderstanding. The statement should have read: 'The authors declare competing financial interests: details accompany the paper on *Nature*'s website (http://www.nature.com/nature).' The details on the website should have read: 'O.L.K. and N.D. have a personal financial interest in Nion, R&D.'. We (the authors) had no intention of misrepresenting the origin of the work. □